Mechanisms limiting the release of TiO 2 nanomaterials during photocatalytic cement alteration: the role of surface charge and porous network morphology

Nathan Bossa, Perrine Chaurand, Clément Levard, Jérôme Vicente, Daniel Borschneck, Christophe Geantet, Olivier Aguerre-Chariol, Jérôme Rose

Mechanisms limiting the release of TiO 2 nanomaterials during photocatalytic cement alteration: the role of surface charge and porous network morphology

Nathan Bossa, Perrine Chaurand, Clement Levard, Jérôme Vicente, Daniel Borschneck, Christophe Geantet, Olivier Aguerre-Chariol, Jérome Rose

Mechanisms limiting the release of TiO_2 nanomaterials during photocatalytic cement alteration: the role of surface charge and porous network morphology

Nathan Bossa[1,2*], Perrine Chaurand[1], Clément Levard[1], Jérôme Vicente[3], Daniel Borschneck[1], Clément Levard[1], Christophe Geantet[4], Olivier Aguerre-Chariol[2], Jérôme Rose[1]

1- Aix Marseille Univ, CNRS, IRD, INRA, Coll France, CEREGE, Aix-en-Provence, France
2- INERIS (Unités NOVA), Parc Technologique Alata, BP2, 60550 Verneuil-en-Halatte, France
3- Aix Marseille Univ., CNRS, IUSTI UMR 7343, 13013 Marseille, France
4- IRCELYON UMR5256 CNRS- Université Lyon 1, 2 Av. A. Einstein, 69626 Villeurbanne Cedex.

Keywords: Life cycle, exposure, pore throat size, micro and nano X-ray computed tomography (micro and nano-CT), 3D imaging.

Abstract:
Nanomaterials have been widely used in a wide range of manufactured products in order to improve / add new properties. Photocatalytic cement maintains clean and white wall fronts and also provide interesting air pollution-reducing properties due to photocatalytic activity of incorporated TiO_2-NMs. However, despite these environmental benefits, there is evidence of the release of TiO_2-NMs during cement use. Therefore, it is crucial to understand the parameters controlling TiO_2-NMs release. Zêta potentials of TiO_2-NMs were investigated from the unaltered core to the cement altered surface using simulated cement pore waters. The mineralogy and chemical composition of the altered layer were investigated using X-ray Diffraction (XRD) and micro X-ray fluorescence spectroscopy (micro-XRF). Finally, pore network morphology was fully analyzed using X-ray computed tomography at both micro and nano-scales (micro and nano-CT) and quantified using 3D morphological software (i-Morph).
This study provides evidence that the TiO_2-NMs release comes from a very thin "active surface layer" (thickness less than 20 µm) where both cement surface chemistry and the pore network appears to be favorable for the TiO_2-NMs diffusion. The pore volume connected to the surface with a throat size ≥1016 nm appears to control and be used as a predictor for TiO_2-NMs release.

1.1 Introduction

The industrial scale production and wide variety of applications of manufactured nanomaterials (NMs) have sparked concern among the nanotechnology and environmental science community because of their potential release into the environment. [e.g.1–3] Products in which NMs are incorporated (nano-products) are considered to be the main potential source of NM release into the environment. [e.g 4–6] However in a global NMs exposure scenario, the entire life cycle of a nano-product has to be considered. In the specific case of the use phase, release scenarios of NMs into the environment is not only a function of the application domain and the way the nano-product is used.[7] According to Hansen et al.[8], NMs release is influenced by the type of nano-product matrix (solid, liquid or aerosol) and NMs incorporation strategy (surface or bulk). The experimental approach to predict NMs release during the use phase consists in simulating lab-scale aging and degradation of nano-products in accelerated conditions and the quantification of NMs release in eluates. The challenge is then to extrapolate lab-scale release results to realistic conditions characterized by slower aging kinetics under variable and non-saturated natural conditions.[4,9] One way to overcome this difficulty is to identify and quantify parameters controlling NM release from nano-products for modeling purposes. The release mechanisms identified at lab-scale can then be implemented in a model that can be used for predictions of NM release by extrapolating a realistic use-phase. This approach is one of the most challenging aspects of nanotechnology: risk forecasting. However, it remains crucial if NMs and nano-products manufacturers and users, aim to develop a "safer-by-design" approach and to reduce NM exposure and associated impacts.[10]

Cement containing TiO_2 NMs, also called 'self-cleaning cement' and/or "photocatalytic cement", belong to one of the four "Hansen" classes (NMs in the bulk of a solid matrix) with an estimated European annual use of 100 tons of TiO_2 nanomaterials (TiO_2-NMs)[11,12]. Photocatalytic cement maintain clean and white wall fronts[13] and also provide interesting air pollution-reducing properties.[14–17] These properties are due to the photocatalytic property of TiO_2-NMs incorporated in the cement matrix. Under UV radiation, TiO_2-NMs can oxidize and/or reduce (i.e. degradation) compounds adsorbed at the cement surface (organic compounds as well as gaseous molecules).[18]

Exposure to TiO_2-NMs can potentially occur at the various stage of the cement life-cycle. This study will exclusively focus on the use stage for the potential release of TiO_2-NMs and exposure of the environment was identified. Indeed, it is well known that the cement matrix is altered when exposed to weathering conditions (e.g. rain draining on cement wall). An altered layer is then formed at its surface where numerous and complex reactions occur such as cement phase congruent or incongruent dissolution, secondary phases precipitation,

etc...[19–22] This altered layer is characterized by an increase of porosity and the presence of altered mineralogical fronts from the cement surface to the unaltered core.[23–25]

Our recent study aimed at quantifying TiO_2-NMs release during the use stage of the photocatalytic cement.[26] In this regard, we have performed a lab-scale leaching test on three photocatalytic cement with three different initial porosities. Particulate and soluble Ti releases were measured at each stage. As anticipated, only particulate TiO_2-NMs were released from cement with a relatively low release rate. We hypothesized that increasing initial porosities would lead to the increased degradation rate of the cement matrix and therefore increased TiO_2-NMs release. Cement matrix degradation rates were measured from the altered layer thickness and porosity measurements over leaching time. As expected, the cement degradation rate was controlled by initial cement porosity, but the mechanisms controlling TiO_2-NMs release appeared to be more complex than initially suspected. Cumulated TiO_2-NMs release from cement with the lowest degradation rate (corresponding to the sample with the lowest initial porosity) reached 18.7± 2.1 mg of Ti/m^2 of cement and remained significantly below the release observed for the two others cements (medium and highest initial porosity) measured at 33.4 ± 7.1 mg of Ti/m^2 of cement. This lab-scale data estimates the simulation between up to 10 years of cement aging during use.

The initial porosity and degradation rates (altered layer thickness and porosity increase) were not the only parameters to consider for predicting TiO_2-NM release. In particular, we hypothesized that the diffusion of TiO_2-NMs within the pore network of the cement surface can be slowed down or inhibited through two processes: (i) electrostatic interactions between TiO_2-NMs and the cement matrix that will drive the adsorption/desorption of the particles on the cement matrix surface and (ii) size exclusion retention processes related to the pore network morphology that can potentially exhibit physical barriers (i.e. pore connectivity and pore throat sizes).

In this context, this study aims at investigating whether electrostatic interactions or pore network morphology are critical parameters that control TiO_2-NMs release to the environment during cement aging.

Zêta potentials of TiO_2-NMs were investigated from the unaltered core to the cement altered surface using simulated cement pore waters. The mineralogy and chemical composition of the altered layer were investigated using both X-ray Diffraction (XRD) and micro X-ray fluorescence spectroscopy (micro-XRF). Finally, pore network morphology was fully described using X-ray computed tomography at both the micro and nano-scale (micro and nano-CT) and quantified using 3D morphological software (i-Morph).[27] Powerful quantitative operators were specifically developed for this study.

1.2 Methods

1.2.1 Alteration of cement pastes

Cylindrical pellets of hydrated cement paste were prepared and leached at lab-scale following the protocol described in Bossa et al., 2017.[26] The tested anhydrous photocatalytic cement was provided by an industrial partner that incorporated 2.85 wt.% TiO_2-NMs in the cement matrix. Three types of hydrated and hardened cement paste with increasing initial porosity were obtained by mixing anhydrous cement powder with ultrapure water (UPW) at various water-to-cement mass ratios (w/c ratio) set at 30, 40 and 50%. Hydrated cements were named cement 30, 40 and 50% respectively. A 7-day batch-leaching test was then performed to simulate the cement aging during its use stage and to quantify TiO_2-NMs release kinetics.

Details about the altered sample preparation is available in Figure S1.

1.2.2 TiO_2-NMs Zêta potential in simulated cement pore water

To assess the TiO_2-NMs surface properties in cement pore water, aqueous dispersions of 100 mg/L were prepared from commercialized powdered TiO_2-NMs (Alfa-Aesar 39953, anatase, particle size of 32 nm). The TiO_2-NMs concentration was chosen to obtain a detectable signal for Zêta potential measurement.

Powdered TiO_2-NMs were dispersed in alkaline Ca-rich solutions with ionic strengths (I) varying from 0.5 to 10 mmol Ca/L (Ca was added as $CaCl_2.2H_2O$) and pHs ranging from 10 to 13 (using a 1N NaOH solution addition). These solutions simulated cement pore water composition along the alteration mineralogical front. [26,29,30] Zêta potential of this TiO_2-NMs suspension was obtained by laser Doppler electrophoresis (Nanosizer NanoZ, Malvern Instruments).

1.2.3 Mineralogical analysis by X-ray diffraction (XRD)

Mineralogical composition of the altered layer was determined by XRD using a PANalytical X'Pert-Pro powder diffractometer equipped with a cobalt source (λ=1.79 Å) and operated at 40 kV and 40 mA. After 7 days of leaching, altered cement pellets were dried under a N_2 atmosphere to prevent secondary surface carbonation. Then the altered layer was separated from the unaltered core by a smooth polishing of the pellet surface (using a sanding paper with a grain size of 200 µm). Powders obtained from the altered layers were then ground with an agate mortar and analyzed by XRD with a counting time of 10 s per 0.04° step in the 6-80° 2θ range.

1.2.4 Hyperspectral mapping of the alteration layer

7-day altered cement pellets were coated with epoxy resin (araldite AY 103 mixed with hardener Hy 956) to preserve the structure of the very porous and friable altered surface layer prior to hyper-spectral mapping (details are given in Figure S1).

Hyper-spectral chemical mapping was carried out using a micro X-ray fluorescence spectrometer (micro-XRF; model XGT-7000, HORIBA Jobin Yvon) equipped with an X-ray guide tube producing a finely focused beam with a 10 µm spot size (Rh target, accelerating voltage of 30 kV, 1mA). Chemical maps (256 x 256 pixels with a pixel size of 10 µm) showing the spatial distribution of Ti, Si and Ca were obtained from their respective Kα emission lines with a total counting time of 20000s/map. Mapping areas were selected on a cross-section of embedded leached cement pellet including the unaltered core, the altered layer and, the cement-water interface. Ca and Si profiles (expressed as XRF intensity of Kα line) along the x-axis (step size of 10 µm) from cement surface to unaltered core along the altered layer was extracted from a hyperspectral map with ImageJ free software.[30,31] XRF intensity profiles of layers were obtained by integrating at least 100 pixels along the y-axis.

1.2.5 3D imaging of cement pore network by coupled micro and nano X-ray computed tomography (micro and nano-CT)

The quantification of the cement pore volume is a complex task and is usually performed by mercury intrusion porosimetry (MIP) for its ability to quantify almost all cement pore size ranging from a few nm to 375 µm.[31,32] However, MIP provides only bulk information restricting the microstructure gradient assessment along the altered layer. A methodology that combines micro- X-ray computed tomography (CT) and a new generation of laboratory-based nano-CT [32,33] (i.e. voxel size of 63.5 nm) to perform a detailed characterization of the pore network of both the altered and unaltered cement (pore size from 130 nm up to ten µm) was recently introduced and detailed by Bossa et al.[25, 26].

For micro and nano-CT analysis embedded leached cement pellets were cut perpendicularly to the cement surface into sticks (5X5X15 mm and 0.4X0.4X15 mm for micro and nano-CT scan, respectively). Obtained sticks are cross-sections of the cement sample including three layers: the unaltered core, the altered layer and the epoxy resin (details are given in Figure S1).

Micro-CT scans were carried out using a microXCT-400 X-ray microscope (Zeiss Xradia) to determine the cement porosity with pore size larger than 3.62 µm (>2 voxels) on a large field of view (FOV) of mm size range, i.e. a representative sample volume including the unaltered core, the altered layer and the resin. Scans were performed at 60 kV (W target) and 150 µA with 1601 projections (angle step of 0.225° from -180 to 180°) and a 6 s exposure time per projection for a total scan time of 4 hours including the collection of reference images. The isotropic voxel size achieved under these conditions was 1.81 µm (x=y=z) and the FOV was 1.85 mm (x=y=z).

Nano-CT scans were obtained using an UltraXRM-L200 X-ray microscope (Zeiss Xradia). The spatial resolution of this equipment is unique at the laboratory scale and reaches 150 nm

using a Fresnel zone plate to focus the transmitted beam on a scintillator plate in front of a 20X optical device. A copper (Cu) X-ray source (rotating anode) produces a polychromatic beam with a maximum intensity at the energy of 8.048 keV (Cu Kα X-ray emission line). Scans were recorded with 901 projections from -90 to 90° with an angle step of 0.16° and an exposure time of 40 s per projection for a total scanning time of 12 hours per FOV including the collection of reference images. The corresponding optical magnification is 200 with a voxel size of 63.5 nm and a FOV of 65 µm (x=y=z). Thus nano-CT allows characterization of pore network including pore size from 130 nm (>2 voxels) to 65 µm. Nano-CT FOV was centred at the interface between cement and resin and including an altered layer depth of 35 µm. In this FOV, the cement surface exposed to the environment was 1584 μm^2.

Stacks of 2D reconstructed slices (3D micro and nano-tomograms) were computed using a smoothing filter (kernel size of 0.7 and 1.2 for the micro and nano-CT, respectively). A full description of the reconstruction procedure can be found in Bossa et al.[25].

1.2.6 Pore network morphological parameters quantification

Reconstructed micro and nano-CT data require 3D image treatment and analysis to obtain quantitative information on pore network morphological parameters. The complete data-treatment process of reconstructed volume was developed in a previous study.[25] Briefly summarized, it includes a filtering and thresholding step to obtain a segmented binary volume to differentiate voids (pores) (voxels with an assigned value of 1) from solid matrix (cement phases) (voxels with an assigned value of 0).

The pore connectivity was investigated from this binary volume. Two pores (void volume) are assimilated as connected if they share a minimum of two voxels. The volume percentage of connected pore is calculated by dividing the volume of the largest connected pore to the total void volume. A pore connectivity of 100% signified that all voids are connected to one another.

The pore size distribution was assessed using the granulometric i-Morph operator.[35,36] For every voxel in the void phase, the operator measured the diameter of the maximal ball included in the void phase at this position (i.e. containing this voxel). The diameters of balls are indexed to obtain the granulometric volume distribution of the void phase (Figure S2.).

A new 3D operator (named “accessible pore” operator) was developed and implemented under the i-Morph software to quantify the pore volume connected to the cement surface as a function of the throat size by which it is connected to the surface. The throat or throat size corresponds to the channel size between two pores.[36,37] 3D operators measuring separately these 2 parameters, i.e. pore volume connected to the cement surface and throat size, are available in the literature.[37–40] To the best of our knowledge, it is the first time that an operator correlates these 2 parameters.

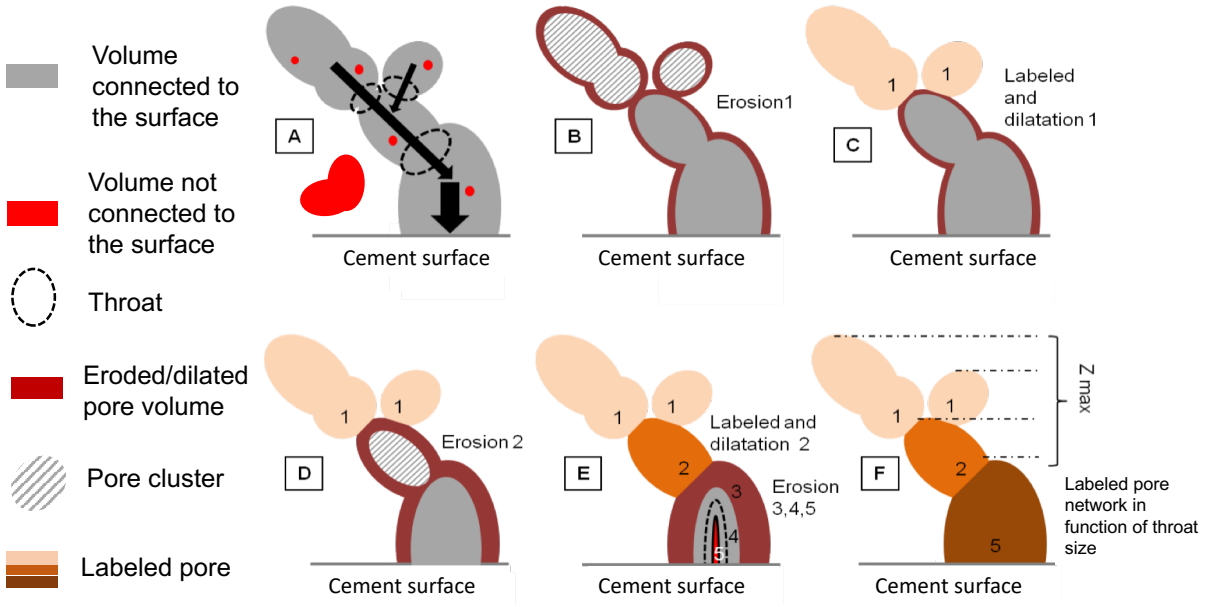

Figure 1 : Schematic view of the "accessible pore" i-Morph operator steps, processed on nano-CT binary volume (void volume), pore cluster refer to pore disconnected to cement surface after an erosion step.

The developed operator is a succession of erosion, labeling, dilatation and quantification steps on a binary volume showing the void phase (i.e. cement porous network in this study). The pore volume first undergoes an image data-treatment that eliminates any pore volume that is not connected to the cement surface (Figure 1.A). Then, in order to extract information of the throat size, the pore volume connected to the surface is eroded by one voxel in every spatial direction (Figure 1.B). The void volumes disconnected to the cement surface by the erosion step (1 voxel in every direction so 2 voxels size) are then labeled to be distinguished (Figure 1.C) from the pore volume still connected to cement surface. This means that the labeled pore volume that was previously connected to cement surface by a throat of 1 or 2 voxel size (representing a size of 63.5 or 127 nm for nano-CT datasets) can be now quantified. The pore volumes (labeled and unlabeled) are then dilated by 1 voxel in every direction (Figure 1.C) in order to come back to the initial pore volume. Then the labeled pore volume connected to the cement surface is measured. This erosion/dilatation procedure is repeated with a n voxel and iteratively applied until the entire pore volume is eroded. As an example, the erosion step 2,3,4,5 is an erosion of 2,3,4 and 5 voxels in every direction means that the pore volume disconnected during this erosion step was connected to cement surface by a throat size of 190.5-254, 317.5-381, 444.5-508 and 508-635 nm, respectively (Figure 1, D-F). The operator is now implemented in the iMorph software version 3.101 (freeware).[27]

1.3 Results and discussion

1.3.1 Chemical and mineralogical evolution along the altered layer.

The studied cements are composed of two major elements, Ca and Si (see table S1). The micro-XRF intensity profiles of these two major elements along the altered layer of the three cements, i.e. from the unaltered core to the cement surface, can be used to localize the different alteration zones. The Ca/Si ratio was calculated in this study to interpret the dissolution front along the altered layer (Figure 2).[40,41]

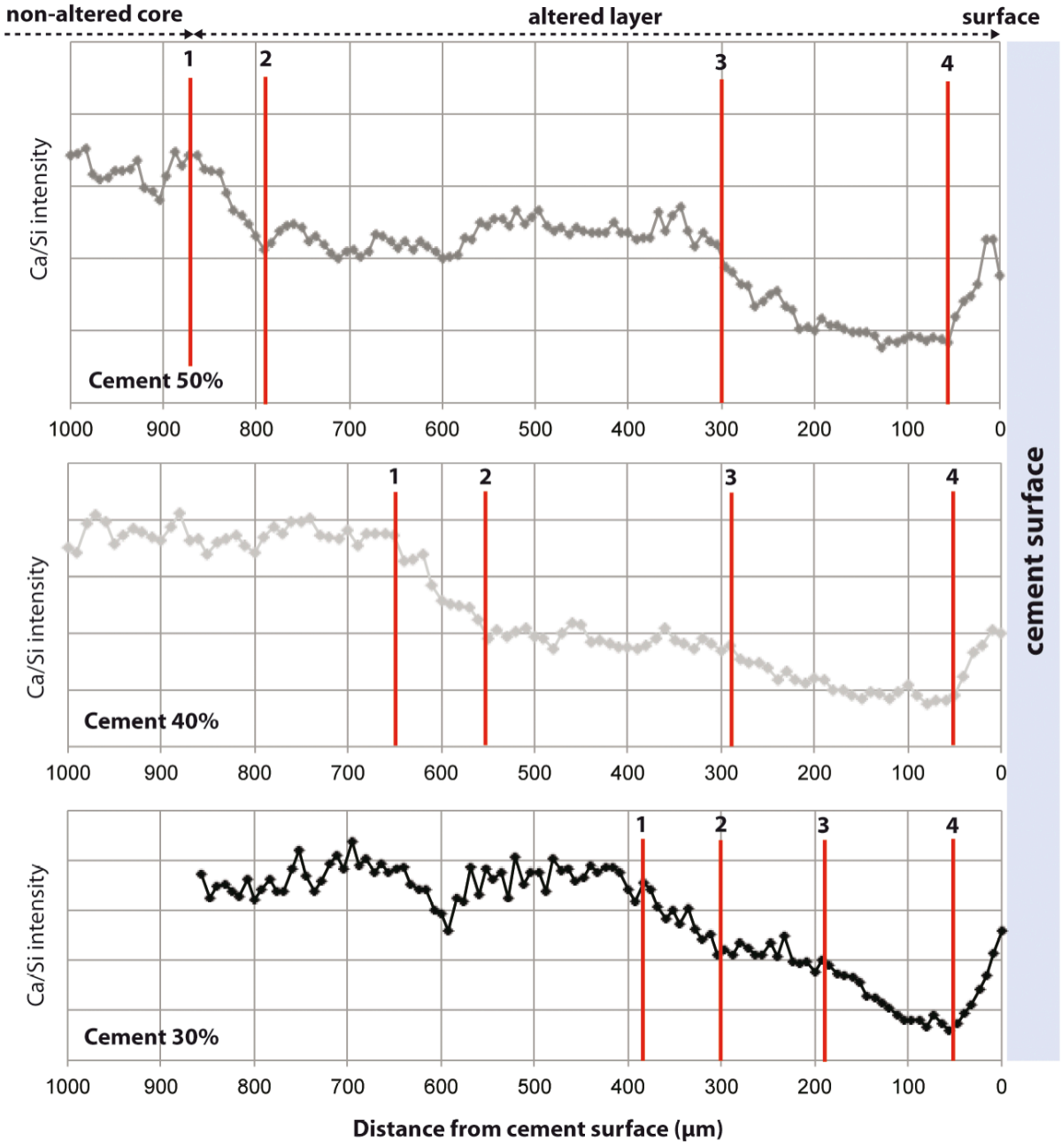

Figure 2 : Evolution of Ca/Si intensity ratio obtained from hyper-spectral micro-XRF maps along the altered layer of cement 30, 40 and 50%. Limit 1 represents the interface of the non-altered core and the altered layer. Limit 2 represents the

portlandite dissolution front. The zone between limit 3 and limit 4 corresponds to the C-S-H decalcification zone.

Starting from the unaltered core, the Ca/Si profiles were initially constant, only influenced by mineralogical heterogeneity (from non-altered core to limit 1, Figure 2). For the three initial cements (named, cement 30%, 40% and 50%) two major phases were identified by XRD: calcium silicate hydrates $(CaO)(SiO_4)(H_2O)_4$ (C–S–H according to cement research community notation) and portlandite ($Ca(OH)_2$). Minor phases such as ettringite ($Ca_6Al_2(SO_4)_3(OH)_{12}.26H_2O$) and residual anhydrous minerals $(CaO)_3(SiO)_2$ and $(CaO)_2(SiO)_2$ (C_3S and C_2S in cement notation, respectively) were also detected.

The non-altered core zone was followed by 2 Ca/Si drops and an increase near the cement surface.

1) The first Ca/Si ratio drop (between limits 1 to 2, Figure 2) was associated with a preferential release of Ca due to portlandite dissolution. This drop was observed at 300, 550 and 780 µm from the cement surface of the leached cement 30, 40 and 50 % respectively.

2) The initial drop was then followed by a second Ca/Si plateau where Portlandite was assumed to be totally dissolved.[41,42]

3) The second Ca/Si drop (between limits 3 to 4, Figure 2) was considered to be associated with the C-S-H decalcification[41,42] that occurred 180, 280 and 300 µm from the cement surface of leached cement 30, 40 and 50 µm, respectively.

4) The increase near the cement surface was associated with the secondary precipitation of calcite ($CaCO_3$)[22,42-44] that occurs exclusively during leaching time as precautions were implemented at the end of leaching to avoid its formation. XRD data confirmed the absence of portlandite and the presence of calcite at the cement surface (Figure S3). Details about cement minerals' evolution along the altered layer of Portland cement can be found in other sources.[19]

1.3.2 Zêta potential (ζ) of TiO_2-NMs along the altered layer.

The TiO_2-NMs ζ was measured in cement pore waters simulating the different alteration conditions described above and the alteration of cement was characterized by cement mineral dissolution/reprecipitation, pH decrease in the pore water, and ionic species gradients from the core to the cement surface.[21] The portlandite dissolution and C-S-H decalcification occurred with a Ca concentration in the pore water lower than 20 and 2 mmol/L.[44,45]

Portlandite dissolution conditions were simulated using a 'lime water' solution characterized by a pH of 11.8 and a [Ca] of 10 mmol/L(e.g. [29,30]). The measured *ζ* of TiO_2-NMs dispersed in this solution was -56±4.2 mV. In conditions where portlandite has completely dissolved,

cement pore water can be simulated with a solution characterized by a pH of 10.9 and a [Ca] of 2 mmol/L, the ζ of TiO_2-NMs was -48±5.1 mv. Under C-S-H decalcification conditions ([Ca]=0.5 mmol/L, pH 10.3,), the ζ of TiO_2-NMs was -31.3 ± 2.5 mV.

These results support that the ζ of TiO_2-NMs suspended in pore water will always be assumed to be negative along the altered layer of leached cement.

1.3.3 Affinity of TiO2-NMs toward cement minerals along the altered layer.

TiO_2-NMs attachment to cement mineral surfaces will be promoted when their respective ζ potentials are of opposite values limiting the diffusion of the particles within the pore network. On contrary, when ζ are both negative or both positive and with absolute values larger than approx. 10-20 mV,[45-47] repulsion will occur promoting the diffusion of TiO_2-NMs within the pore network.[48]

Because, there are no technical options to perform in-situ (in the cement paste) measurement, the zeta potential of altered cement minerals was assessed using ex-situ literature values. Pointeau et al.[44,45] studied the ζ potential of cement minerals at different alteration stages. As mentioned above, the ζ potential of cement minerals in the altered layer is mostly controlled by pH and Ca concentration in the pore water released from the dissolution of primary minerals. In particular, ζ potential is controlled by the deprotonation of C-S-H surface sites (>SiO) and by the sorption of calcium on deprotonated sites (>SiOCa+). In the unaltered cement core (pH>13), the amount of dissolved Ca in solution is too low to allow the positive charge of the >SiOCa+ surface site to balance the negative charge of >SiO− site, leading to a net negative ζ potential (Figure 3).

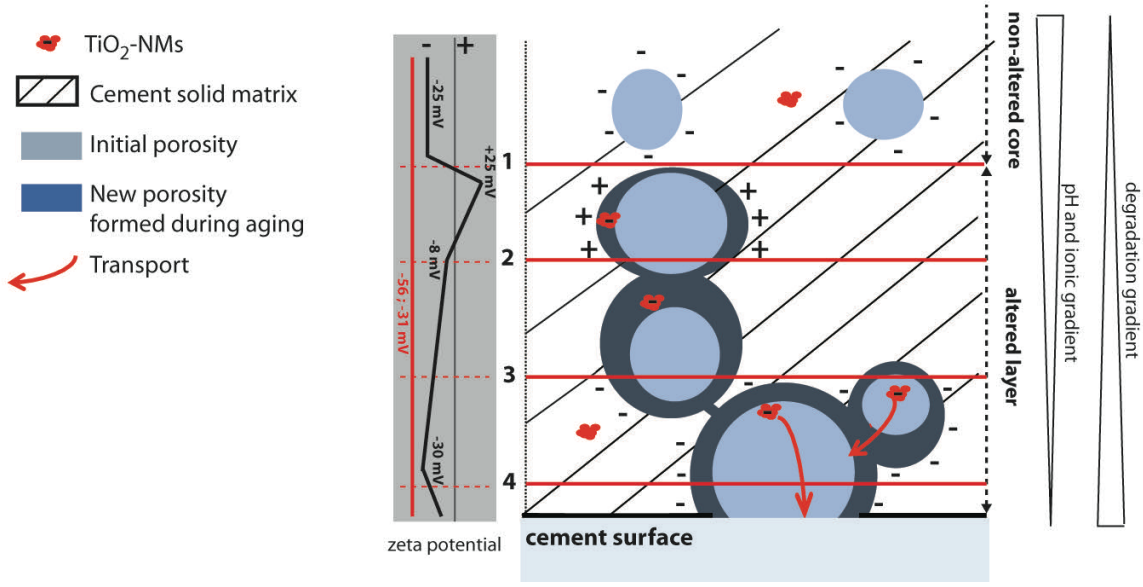

Figure 3 : Schematic view of the electrostatic affinity of TiO_2-NMs to cement minerals along the altered layer.

During the first degradation stage, characterized by a pH decrease, the decrease of hydroxide concentration in solution allows a sufficient release of Ca from portlandite to induce a mean positive ζ potential, with a maximum of +25 mV at pH 12.65. During further alteration with pH between 12.65 and 11, the portlandite dissolution continues until total dissolution. The cement minerals ζ potential slowly decreases from +25 to −8 mV (at pH 11.0), with an isoelectric point (IEP) close to pH 11.7. At pH 11, complete dissolution of portlandite lead to reduce the Ca stock. As a consequence, the >SiOCa+ sites of C-S-H are progressively decalcified. Viallis-Terrisse et al.[47-49] and Labbez et al.[48-50] quantified the ζ potential measurement of C-S-H as function of the concentration of soluble Ca. Their results are in accordance with Pointeau et al.[4445] for [Ca] ≥ 2 mmol/L but additionally, they showed that C-S-H ζ potential highly decreased for [Ca] below 2 mmol/L. Under these conditions, C-S-H is decalcified and the density of >SiO− site increased relatively. With a [Ca] in the percolating water of 0.5 mmol/L, the C-S-H reached a negative ζ potential of -30 mv.[48-50] Micro-XRF profiles showed a calcification front of 50 µm at altered cement surface due to calcite secondary precipitation. No surface charge is theoretically present at the calcite surface. However, calcite defects (i.e. element substitution, element exchange with the ionic solution or hydrolysis and protonations of calcite surface) are supposed to induce charge, when detected and are quantified an always-negative surface charge at calcite surface according to Moulin et al.[49-51]

To summarize, in the zone between limit 1 and 2 where portlandite is dissolved (Figures 2 and 3), the *ζ* potential of cement minerals is estimated to decrease from + 25 mV to -8 mV at limit 2. Therefore in this region, the TiO_2-NMs attachment on cement minerals is highly probable as TiO_2-NMs *ζ* potential is always significantly negative along the altered layer. From limit 2 to 3 (Figure 2 and 3), the *ζ* potential of cement minerals remain negative but with an absolute value around 10 mv, that may not be high enough to promote TiO_2-NMs repulsion from the surface of cement minerals. From limit 3 to 4, as C-S-H release Ca^{2+} in the pore water, the *ζ* potential decreases significantly to reach almost -30 mV at limit 4. In that zone TiO_2-NMs and cement mineral surface are both negative and electrostatic repulsions can occur. We hypothesis that a more restricted altered layer (i.e. a layer thinner than total altered layer) contributes to the diffusion of TiO_2-NMs suspended in the cement pore network into the environment. Of course the zeta potential is only a proxy to predict nano-TiO_2 attachment and cannot be considered as a direct measurement such as surface affinity (α) measurement.

Interestingly the thickness of this “diffusion” layer is of the same order of magnitude for cement 40 and 50% (≈300µm) despite different total altered layer thicknesses (Figure 2) while this layer for cement 30% is significantly thinner (180µm). This is in good accordance with the TiO_2-NMs release trends observed and summarized in S.I. (Figure S4). The *ζ*

potential appeared to be a credible parameter that will potentially control the release of TiO_2-NMs out.

1.3.4 Retention of TiO_2-NMs in the cement porous network by size exclusion mechanism (physical retention)

1.3.4.1 Pore connectivity and pore size distribution within altered cements

In addition to the electrostatic interactions between TiO_2-NMs and the cement matrix, physical barriers can also strongly impact the diffusion of those particles within the pore network and the environment. These physical parameters include pore size distribution, pore connectivity throat size (pore space connecting two larger pore volumes) distribution and pore volume connected to the cement surface that we propose to investigate in the following section.

Two structural parameters of the pore network, i.e. pore connectivity and pore size distribution were measured by coupled micro-CT and nano-CT. However, the size exclusion mechanism was only investigated from the nano-CT measurements as the resolution of the micro-CT provided a partial analysis of the pore network that included only the largest pores. ~~N~~nano-CT measurements enabled to determine the morphology of smallest pores down to at least 130 nm.

These two structural parameters were then compared to the size of TiO_2-NMs dispersed in cement paste in order to estimate whether the diffusion of TiO_2-NMs through the pore network was possible using a simple geometric consideration.[51,52]

In a previous study[28], partial data on TiO_2-NMs size distribution were obtained by TEM observations before their incorporation in anhydrous cement powder but the behavior of the TiO_2-NMs agglomerates and unit particles during cement hydration remained unknown. TiO_2-NMs were found to exhibit a unit size from 55 and 270 nm (mean size = 138 ± 53 nm, N: 35) and agglomerates with a size up to 500 nm were also observed. However, the size distribution of TiO_2-NMs in the cement paste was impossible to estimate using TEM-EDX because of the low contrast of TiO_2-NMs with cement minerals and the size of the EDX spot. The following discussion on size exclusion mechanisms was not based on a direct size cut-off so it was only assumed that the TiO_2-NMs were dispersed as both unit particles and agglomerates potentially larger than 500 nm in hydrated cement pastes.

	Pore connectivity	Volumetric % of pores ≥ 254±64 nm	Volumetric % of pores ≥ 508±64 nm
Cement 30%	83 %	72%	13%
Cement 40%	96 %	90%	64%
Cement 50%	99 %	99%	71%

Table 1 : Pore connectivity, Volumetric % of pore ≥ 254 nm and ≥ 508 nm in the altered layer of cements 30, 40 and 50% as measured by the granulometric i-Morph operator obtained from nano-CT measurements (FOV centred at cement surface).

A granulometric i-Morph operator was used to calculate the granulometric volume distribution of pores. The pore size corresponding to the median, seven deciles and nine deciles of the total pore volume of the altered layer are listed in **Erreur ! Source du renvoi introuvable.** for the three cement types.

Strong differences between the three cement types are observed. The volumetric % of pores ≥ 254 nm represent 72, 90 and 99% of pore volume for cement 30, 40 and 50%, respectively and the volumetric % of pores ≥ 508 nm represent 13, 64 and 71% of pore volume for cement 30,40 and 50%, respectively. Once again, the last two cements exhibit similar pore granulometric volume distributions. With regard to the unit TiO_2-NMs size (55 to 270 nm) and the TiO_2-NMs aggregate size (≈500 nm), only the diffusion of unitary TiO_2-NMs appears conceivable through cement 30% altered layer pore network. While altered pore network of cement 40 and 50% could allow the diffusion (with simple geometric consideration) of both unitary TiO_2-NMs and aggregates.

1.3.4.2 Size of throat between two pores in pore volume connected to the surface

More than pore sizes, the throat size[36,37], the size of the channel connecting two pores, need to be considered since it will strongly control TiO_2-NMs diffusion in the pore network. Also, only the pore volume connected to the surface should be considered or to be more precise, the link between pore volume connected to the cement surface and throat with size above a critical threshold that will let the TiO_2-NMs diffuse to the surface is the strongest correlation between TiO2 NM diffusion and the pore network.

Figure 4 is a schematic view of the modification/evolution of the pore network (pore size and connectivity, throat size) with alteration time and it describes potential TiO_2-NMs release scenario based on geometrical considerations. An increase of porosity after cement degradation due to partial dissolution over aging will create different types of pores that may be potentially involved in TiO_2-NMs diffusion to the environment. Pore A is an isolated pore disconnected to the cement surface where the TiO_2-NMs are retained. Pore B represents a pore connected to cement surface by a throat size blocking the TiO_2-NMs diffusion by size exclusion. Pore C (delimitated with red borders) illustrates a pore connected to cement surface by a throat size allowing TiO_2-NMs diffusion. All three pore types are thus involved in the TiO_2-NMs release into the environment.

This schematic view suggests that the quantification of porosity increase led by cement aging is not accurate enough to predict TiO_2-NMs release. Therefore, more precision on pore network volume involved in TiO_2-NMs release is required. Indeed, the pore network in the altered layer exhibits a complex and heterogeneous morphology with some pores (pore types A and B) potentially blocking TiO_2-NMs diffusion.

Based on the schematic view of Figure 4, it is crucial to compare throat size between two domains/pores and the size of TiO_2-NMs incorporated in the photocatalytic cement matrix.

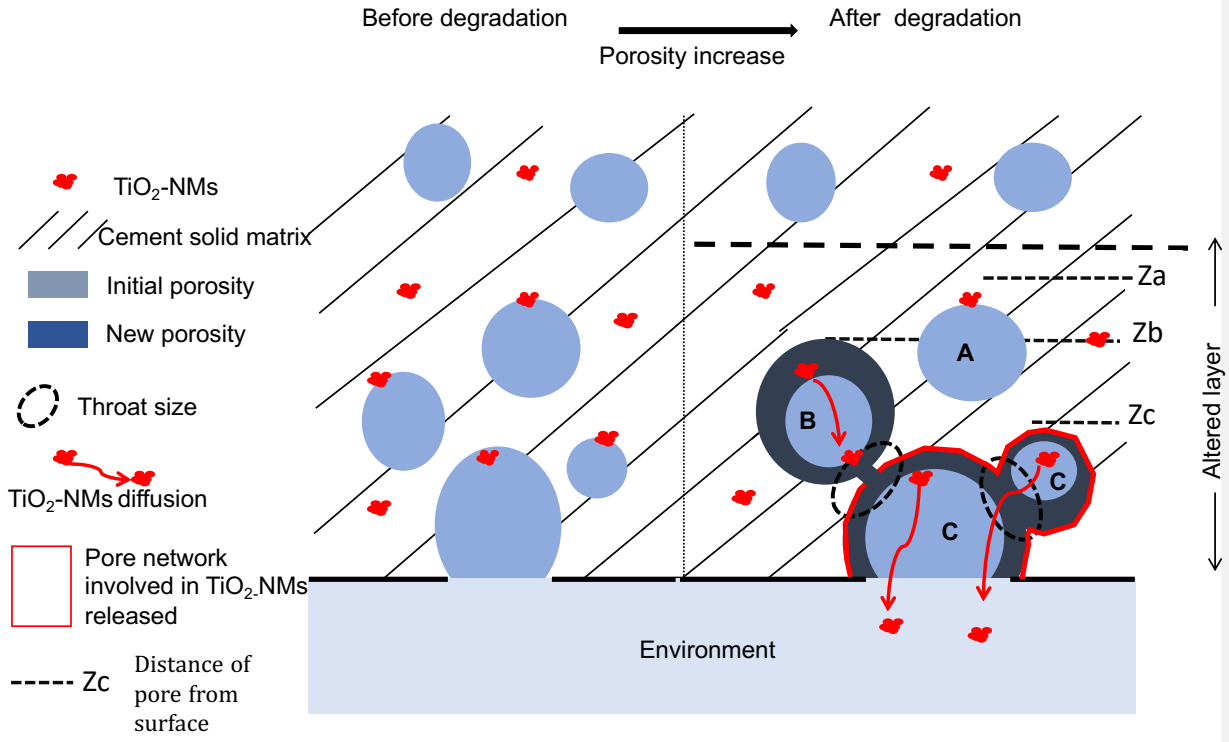

Figure 4 : Schematic view of the cement pore network increasing during degradation and aging. Different types of pores (pores A, B and C) are represented.

Because of the uncertainties of the distribution size of TiO_2-NMs (from 55 up to 500 nm and maybe more), it is difficult to define the critical / threshold throat size that will, or will not, allow the diffusion of the TiO_2-NMs to the surface. However, one can correlate the pore volume connected to the cement surface as a function of its critical throat sizes for the 3 cement types. These data can then be compared to the TiO_2-NMs release kinetics (Figure S4). Such comparison will provide precious information regarding this unknown critical throat size.

"Accessible pore" i-Morph operator was run on nano-CT binary volumes (volume of 64x64x64 µm showing void phase) obtained for cement 30, 40 and 50% with FOV centered at 32 µm to include the cement surface. The pore's volume connected to the cement surface

(expressed in voxel numbers) as a function of their (smallest) throat size is shown in Figure 5.A for the three differing cement types.

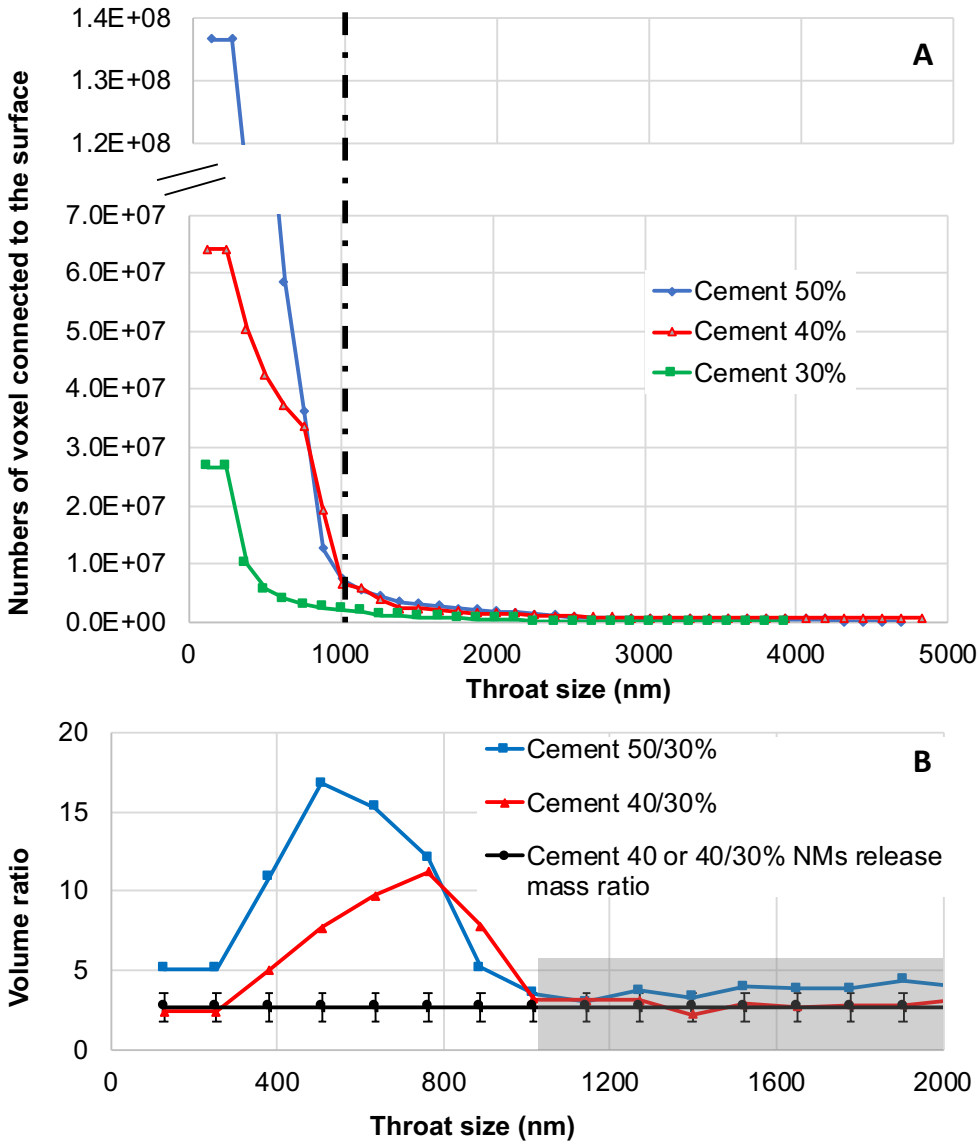

Figure 5 : A) Pore volume connected to the cement surface (expressed in voxel number) as function of the smallest throat size for cement 30, 40 and 50%. Data were obtained by running "accessible pore" i-Morph operator on nano-CT binary volumes. B) Volume ratio of Cement 50%/cement 30% and cement 40%/ cement 30% as function of throat size. The grey curve represent the Ti release (mg of Ti by m^2 of cement) ratio of cement 40 and 50% / cement 30% obtained from cement leaching test after 7 days extracted from figure S4.

Figure 5.B is obtained from the data shown in Figure 5A by dividing cement 50% and cement 40% curve by cement 30% curve to obtain volume ratio as function of the smallest throat size. We assumed that the Ti released mass is proportional to the volume of the pore

connected to the cement surface. Volume ratios were compared to Ti release experimental results obtained in Bossa et al., 2017.[26] As mentioned above total Ti release was found to be similar for cements 40 and 50 % and higher than Ti release observed for cement 30%. Ti release mass ratio was calculated from the total mass of Ti released measured during the 7-day leaching test for cement 50% (or 40%) and cement 30%. The obtained (cement 50% or 40%/cement 30%) Ti release mass ratio was of 2.7 ±0.44 (grey line in Figure 5B). One can then define a critical throat size of 1016 nm or above in which the (Cement 50% or Cement 40%)/Cement 30% volume ratios are almost similar to the observed Ti release (cement 50% or 40%)/Cement 30% mass ratio (2.7 ±0.44) (grey zone in Figure 5.B). Moreover, the cement 50%/cement 30% and cement 40% / cement 30% volume ratios well superimposed for throat size higher than this critical value of 1016 nm (Figure 5.A). Furthermore, the critical throat size is superior to the estimated unitary and aggregate NMs size.

We can, therefore, hypothesize that the pore volumes connected to the surface with throat size larger than 1016 nm contribute to the diffusion and release of TiO_2-NMs. The smaller pore volume connected to the surface with a throat size ≥1016 nm in the altered layer of cement 30% can explain why there is a much lower release of TiO_2-NMs during alteration for 30% rather than for cement 40% and 50%.

1.3.4.3 Thickness of the “active surface layer” (size of the altered cement layer contributing to the diffusion and release of TiO_2-NMs into the environment)

Further description of the throat size parameter was performed by investigating its 3D spatial distribution in terms of its maximum penetration depth from the cement’s surface. The measure of the maximum Z value for each labeled pore volume connected to cement surface was implemented into the “accessible pore” i-Morph operator (Figure 1). Z was defined as the maximum distance of the labeled pore volume from the cement surface (or the penetration depth). Then the acquired z value was plotted vs. throat size as shown in Figure 6 below.

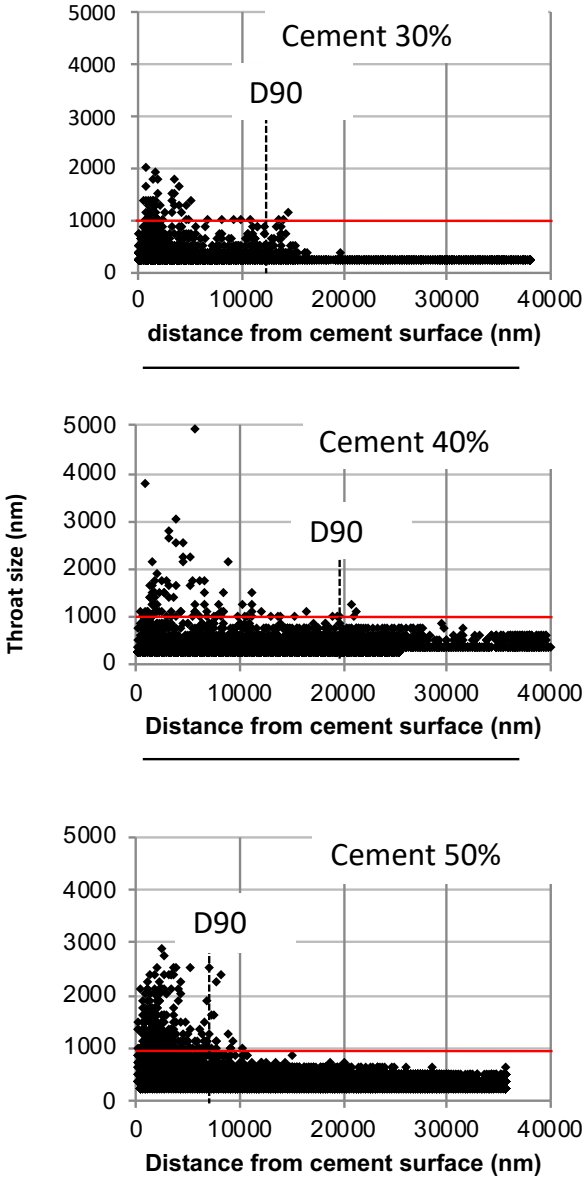

Figure 6 : Maximum penetration depth (maximum distance from cement surface) of each labelled pore volume (i.e. pore volume connected to cement surface) as function of their throat size for the three cement types (cement 30, 40 and 50%). The red lines show the throat size of 1016 nm, identified as the size controlling the TiO_2-NMs diffusion into altered cement porous network towards the surface. D70 (dotted lines) represents the maximum distance from surface including 90% (night deciles) of labelled pore volume connected to surface by a throat ≥ 1016 nm.

In Figure 6, each symbol (180, 440 and 525 labeled pores for cement 30, 40 and 50%, respectively) corresponds to a pore volume connected to the cement surface labeled by the i-Morph operator (Figure 1). The pore volume of every labeled pore was quantified, as well as its smallest throat size and maximum distance from the cement surface. Data obtained

from nano-CT binary volume centered at the 32 µm from surface of altered cement 30, 40 and 50% are shown (Figure 6). For the three cements, the maximum depth of pore volume connected to cement surface decreases with increasing throat size. In other words, the pores connected to the surface by the larger throat size are located to the very near surface. As shown in Figure 6, the pores connected by the proposed critical throat size are largely present only in the first 20 µm. The D90 of the maximum penetration depth of pore volume connected to the surface by the critical throat size (≥1016±64 nm) is 14.1, 19.6 and 7.2 µm for cement 30, 40 and 50%, respectively. These results revealed that there is no correlation between the active surface layer thickness and the total altered layer thickness. This layer represents less than 5% and 10% of the total altered layer and the calculated "diffusion" layer, respectively.

We demonstrated that TiO_2-NMs diffusion within the cement altered layer was controlled by a size exclusion mechanism. A throat size of 1016±64 nm was identified/proposed as the throat size limiting the diffusion of TiO_2-NMs in pore volume connected to cement surface. This morphological parameter appears to be a key factor controlling TiO_2-NMs release and their exposure level during the use stage of photocatalytic cement .
In a previous study[26], the authors' estimated the TiO_2-NMs released potential mass from the quantity of TiO_2-NMs initially dispersed (2.85 wt.%) in the cement matrix, the volume of the altered layer (total altered layer thickness) and the hypothesis of a constant porosity increase along the altered layer. The calculated values reached 2.1, 5.3 and 21.6 g of TiO_2/m^2 of cement for cement 30, 40 and 50%, respectively, and were higher than the experimental release data (experimental release data represent only 0.26-1.43% of the calculated data).
If we use the volume of pore connected to cement surface by the critical throat size (≥1016±64 nm) the calculated values reached 11.5, 48.6 and 49.1 mg of TiO_2/m^2 representing 37, 87 and 88% of measured release TiO_2. This study demonstrated that the release potential during cement aging should be refined based on the identification of a morphological parameter that strongly controls the diffusion and release of TiO_2-NMs. This powerful parameter was identified as the pore volume connected to the surface by a throat ≥ 1016 nm. Therefore, in conclusion, the TiO_2-NMs' release comes from a very thin layer that has a thickness less than 20 µm and is identified as the "active surface layer".

1.4 Acknowledgments

The authors gratefully acknowledge the Provence-Alpes-Côte d'Azur Region (France) and INERIS (Institut National de l'Environnement Industriel et des Risques - France) for financial support. The project leading to this publication has received funding from Excellence Initiative of Aix-Marseille University - A*MIDEX, a French "Investissements d'Avenir"

program, through its associated Labex SERENADE project. The French X-ray CT platform was funded by the Nano-ID EQUIPEX project ANR-10-EQPX-39-01. This work also benefited from the support from the competitiveness cluster ‘Pole Risques’ (Aix-en-Provence – France). The authors gratefully acknowledge Joana Marie Sipe (Duke University) for her active support as an external reviewer of the manuscript.

References

1 D, Hristozov,, I. Malsch, *Sustainability*. 2009, ***1***, 1161-1194

2 M. R. Wiesner, G. V. Lowry, P. Alvarez, D. Dionysiou and P. Biswas, *Environ. Sci. Technol.*, 2006, **40**, 4336–4345.

3 N. O'Brien and E. Cummins, *J. Environ. Sci. Health Part A Tox. Hazard. Subst. Environ. Eng.*, 2010, **45**, 992–1007.

4 F. Gottschalk and B. Nowack, *J. Environ. Monit.*, 2011, **13**, 1145–1155.

5 B. Nowack, C. Brouwer, R. E. Geertsma, E. H. W. Heugens, B. L. Ross, M.-C. Toufektsian, S. W. P. Wijnhoven and R. J. Aitken, *Nanotoxicology*, 2013, **7**, 1152–1156.

6 T. Y. Sun, F. Gottschalk, K. Hungerbuhler and B. Nowack, *Environ. Pollut.*, 2014, **185**, 69–76.

7 B. Nowack, J. F. Ranville, S. Diamond, J. A. Gallego-Urrea, C. Metcalfe, J. Rose, N. Horne, A. A. Koelmans and S. J. Klaine, *Environ. Toxicol. Chem. SETAC*, 2012, **31**, 50–59.

8 F. . Hansen, B. . Larsen, S. I. Olsen and A. Baun, *Nanotoxicology*, 2007, **1**, 243–250.

9 L. Scifo, P. Chaurand, N. Bossa, A. Avellan, M. Auffan, A. Masion, B. Angeletti, I. Kieffer, J. Labille, J.-Y. Bottero and J. Rose, *Environ. Pollut.*, 2018, **241**, 182–193.

10 J. Y. Bottero, J. Rose, C. de Garidel, A. Masion, T. Deutsch, G. Brochard, M. Carrière, N. Gontard, H. Wortham, T. Rabilloud, B. Salles, M. Dubosson, B. Cathala, D. Boutry, A. Ereskovsky, C. Auplat, L. Charlet, T. Heulin, E. Frejafon and S. Lanone, *Environ. Sci. Nano*, 2017, **4**, 526–538.

11 F. Piccinno, F. Gottschalk, S. Seeger and B. Nowack, *J. Nanoparticle Res.*, 2012, **14**, 1109.

12 T. Y. Sun, F. Gottschalk, K. Hungerbuehler and B. Nowack, *Environ. Pollut.*, 2014, **185**, 69–76.

13 B. Ruot, A. Plassais, F. Olive, L. Guillot and L. Bonafous, *Sol. Energy*, 2009, **83**, 1794–1801.

14 R. Sugrañez, J. I. Álvarez, M. Cruz-Yusta, I. Mármol, J. Morales, J. Vila and L. Sánchez, *Build. Environ.*, 2013, **69**, 55–63.

15 C. Cárdenas, J. I. Tobón, C. García and J. Vila, *Constr. Build. Mater.*, 2012, **36**, 820–825.

16 A. M. Ramirez, K. Demeestere, N. De Belie, T. Mäntylä and E. Levänen, *Build. Environ.*, 2010, **45**, 832–838.

17 T. Maggos, A. Plassais, J. G. Bartzis, C. Vasilakos, N. Moussiopoulos and L. Bonafous, *Environ. Monit. Assess.*, 2007, **136**, 35–44.

18 J.-M. Herrmann, *Catal. Today*, 1999, **53**, 115–129.

19 P. Faucon, P. Le Bescop, F. Adenot, P. Bonville, J. F. Jacquinot, F. Pineau and B. Felix, *Cem. Concr. Res.*, 1996, **26**, 1707–1715.

20 S. Kamali, M. Moranville and S. Leclercq, *Cem. Concr. Res.*, 2008, **38**, 575–585.

21 P. Faucon, F. Adenot, J. F. Jacquinot, J. C. Petit, R. Cabrillac and M. Jorda, *Cem. Concr. Res.*, 1998, **28**, 847–857.

22 P. Faucon, F. Adenot, M. Jorda and R. Cabrillac, *Mater. Struct.*, 1997, **30**, 480–485.

23 K. Haga, M. Shibata, M. Hironaga, S. Tanaka and S. Nagasaki, *Cem. Concr. Res.*, 2005, **35**, 943–950.

24 T. Sugiyama, M. A. B. Promentilla, T. Hitomi and N. Takeda, *Cem. Concr. Res.*, 2010, **40**, 1265–1270.

25 N. Bossa, P. Chaurand, J. Vicente, D. Borschneck, C. Levard, O. Aguerre-Chariol and J. Rose, *Cem. Concr. Res.*, 2015, **67**, 138–147.

26 N. Bossa, P. Chaurand, C. Levard, D. Borschneck, H. Miche, J. Vicente, C. Geantet, O. Aguerre-Chariol, F. M. Michel and J. Rose, *Environ. Pollut.*, 2017, **220**, 1160–1170.

27 E. Brun, J. Vicente, F. Topin and R. Occelli, *Cell. Met. Struct. Funct. Appl.*

28 N. Bossa, P. Chaurand, J. Vicente, D. Borschneck, C. Levard, C. Geantet, O. Aguerre-Chariol and J. Rose, *Prep*.

29 S. Garrault-Gauffinet and A. Nonat, *J. Cryst. Growth*, 1999, **200**, 565–574.

30 A. Nonat and X. Lecoq, in *Nuclear Magnetic Resonance Spectroscopy of Cement-Based Materials*, eds. P. Colombet, A.-R. Grimmer, H. Zanni and P. Sozzani, Springer, 1996, p. 197.

31 C. A. Schneider, W. S. Rasband and K. W. Eliceiri, *Nat. Methods*, 2012, **9**, 671–675.

32 R. A. Cook and K. . Hover, *Cem. Concr. Res.*, 1999, **29**, 933–943.

33 A. P. Merkle and J. Gelb, *Microsc. Today*, 2013, **21**, 10–15.

34 E. Maire and P. J. Withers, *Int. Mater. Rev.*, 2014, **59**, 1–43.

35 M. A. B. Promentilla, T. Sugiyama, T. Hitomi and N. Takeda, *J. Adv. Concr. Technol.*, 2008, **6**, 273–286.

36 J. Vicente, Y. Wyart and P. Moulin, *J. Porous Media*, 2013, **16**, 537–545.

37 W. B. Lindquist, A. Venkatarangan, J. Dunsmuir and T. Wong, *J. Geophys. Res. Solid Earth*, 2000, **105**, 21509–21527.

38 S. Lu, E. N. Landis and D. T. Keane, *Mater. Struct.*, 2006, **39**, 611–620.

39 D. Bauer, S. Youssef, M. Fleury, S. Bekri, E. Rosenberg and O. Vizika, *Transp. Porous Media*, 2012, **94**, 505–524.

40 A. P. Jivkov, C. Hollis, F. Etiese, S. A. McDonald and P. J. Withers, *J. Hydrol.*, 2013, **486**, 246–258.

41 M. Mainguy, C. Tognazzi, J.-M. Torrenti and F. Adenot, *Cem. Concr. Res.*, 2000, **30**, 83–90.

42 C. Carde, R. François and J.-M. Torrenti, *Cem. Concr. Res.*, 1996, **26**, 1257–1268.

43 J. Rose, A. Bénard, J. Susini, D. Borschneck, J.-L. Hazemann, P. Cheylan, A. Vichot

and J.-Y. Bottero, *Environ. Sci. Technol.*, 2003, **37**, 4864–4870.

44 P. W. Brown and A. Doerr, *Cem. Concr. Res.*, 2000, **30**, 411–418.

45 I. Pointeau, P. Reiller, N. Macé, C. Landesman and N. Coreau, *J. Colloid Interface Sci.*, 2006, **300**, 33–44.

46 S. Bhattacharjee, *J. Controlled Release*, 2016, **235**, 337–351.

47 D. H. Everett, *Basic Principles of Colloid Science*, The Royal Society of Chemistry, London., 1988.

48 H. Viallis-Terrisse, A. Nonat and J.-C. Petit, *J. Colloid Interface Sci.*, 2001, **244**, 58–65.

49 C. Labbez, I. Pochard, B. Jönsson and A. Nonat, *Cem. Concr. Res.*, 2011, **41**, 161–168.

50 P. Moulin and H. Roques, *J. Colloid Interface Sci.*, 2003, **261**, 115–126.

51 H. J. Vogel, *Eur. J. Soil Sci.*, 2000, **51**, 99–105.

52 G. S. Armatas, *Chem. Eng. Sci.*, 2006, **61**, 4662–4675.